Journal of
Marine Science and Engineering

MDPI

Article

Study on the Damping Effect and Mechanism of Vertical Slotted Screens Based on the BM-MPS Method

Changle Zhang [1,2], Lizhu Wang [1,3,*] and Min Xu [1]

[1] College of Marine Science and Engineering, Nanjing Normal University, Nanjing 210046, China; 27190114@njnu.edu.cn (C.Z.); xumin0895@njnu.edu.cn (M.X.)
[2] First Institute of Oceanography, Ministry of Natural Resources, Qingdao 266061, China
[3] State Key Laboratory of Hydrology-Water Resources and Hydraulic Engineering, Nanjing Hydraulic Research Institute, Nanjing 210029, China
* Correspondence: wlzh2026@163.com; Tel.: +86-02585898551

Abstract: Liquid sloshing is a common phenomenon in ocean engineering, and one which not only affects the stability of ship navigation, but also poses a threat to both the marine environment and human life. Ascertaining how best to reduce the amplitude of liquid sloshing has always been a key problem in ocean engineering. In this study, based on an improved moving-particle semi-implicit method, the BM-MPS method, the damping effect of a vertical slotted screen under rotation excitation was simulated and studied, and the influence of baffle porosity and the rotation amplitude on the resonance period and impact pressure was discussed. The results showed that the porosity had an obvious effect on the resonance period. A significant resonance period transformation happened when the porosity was 0.1, but a porosity of 0.15 was the point at which the maximum impact pressure in the resonance was at its minimum. Meanwhile, the impact duration curve was related to porosity. With the increasing of porosity, the impact duration curve changed from having no peak to a single peak, and then to double peak. In addition, the amplitude of rotation excitation was also one of the factors that affected the resonance period.

Keywords: particle method; liquid sloshing; vertical slotted screen; porosity; rotation amplitude

Citation: Zhang, C.; Wang, L.; Xu, M. Study on the Damping Effect and Mechanism of Vertical Slotted Screens Based on the BM-MPS Method. *J. Mar. Sci. Eng.* **2023**, *11*, 1270. https://doi.org/10.3390/jmse11071270

Academic Editor: Constantine Michailides

Received: 24 May 2023
Revised: 18 June 2023
Accepted: 20 June 2023
Published: 22 June 2023

1. Introduction

Liquid sloshing in fuel tanks is common phenomenon in ship navigation, which adversely affects the stability of the vessel and poses a threat to human safety [1–4]. With the increasing demand for liquefied natural gas (LNG) and liquefied petroleum gas (LPG), there has been a rapid development in large-scale liquid cargo ships. Methods of reducing the degree of liquid sloshing have attracted the attention of many researchers.

One effective method for suppressing sloshing is to install baffles within the liquid tanks; consequently, numerous studies have been conducted on the damping effect of various baffles [5–9]. Previous research has demonstrated that the damping effect of baffles is closely related to the configuration, position, and quantity of baffle, and it has been demonstrated that a vertical baffle has a better sloshing-suppression effect [10–14]. Shao et al. [15] studied the sloshing effect of liquid in rectangular slots with a central, vertically oriented baffle, as well as a horizontal baffle, a "T" baffle, and a porous baffle (in addition to rectangular slots without a baffle), finding that "I" baffle and "T" baffle had a better sloshing reduction effect. Xavier et al. [16] found that the damping effect of a 90° angle was the most significant by designing baffles at multiple angles. Furthermore, it was revealed that the damping effect on sloshing for the baffles with holes was significantly different from that of baffles without holes. [17–19]. Mahammad et al. [20] compared the weakening effect of the perforated baffles and the nonperforated baffles on the impact pressure, pointing out that the perforated baffles performed better at reducing the impact pressure.

Compared with nonperforated baffles, the mechanism of perforated baffles on sloshing suppression is more complicated, owing to the impact of vortex damping. Faltinsen and Timokha [21] studied the variation of frequencies using different submerged screen gaps. Xue et al. [22] studied the square perforated baffle and concluded that the perforated baffle had advantages on suppressing sloshing even if the loading of the LNG tanker increased; by contrast, Hyeon and Cho [23] explored the influence of porosity, submerged depth, and other factors on sloshing suppression, finding that the damping effect was the best when the porosity was 0.1. Poguluri and Cho [24] studied the effect of porosity of vertical baffles. Yu et al. [25] designed solidity ratios of 0.4, 0.6, and 0.9, in order to explore the influence of porosity and slot size on sloshing; they found that a solidity ratio of 0.6 had a better inhibition effect on sloshing. Nasar et al. [26] designed their porosities as 0.15, 0.202, and 0.252, so as to investigate the sloshing pattern during a rolling motion, determining that the best performance was achieved when the porosity was 0.252. Gao et al. [27] explored the optimal effect of sloshing suppression by changing both the pore parameter and the installation form of the porous baffles. Wang et al. [28] analyzed the influence of porous baffles on sloshing under a rotational excitation using numerical simulation, finding that increasing the height of the baffle while decreasing the porosity of the baffle could both enhance the wave-damping. Nimisha et al. [29,30] explored the effect of different porosities on swaying; they concluded that the optimum perforation was within the range of 10~17%. In this range, the porous baffle effectively suppressed the intensity of liquid sloshing on resonance. Arun et al. [31] explored the influence of porous baffles, showing that with the increasing of porosity, the effect of tip-vortices became small. Based on the aforementioned research findings, it is evident that the sloshing suppression effect is obvious when the porosity is small. However, the mechanism by which porosity influences the damping effect has still not been clearly clarified. Furthermore, the majority of studies on perforated baffles have focused on the damping of sloshing induced with horizontal excitation. Consequently, it is worth investigating further the effect and mechanism of perforated baffles on the sloshing suppression under other excitation conditions.

With the rapid development of computer technology, numerical simulation has become one of the most important means for studying liquid sloshing. Liquid sloshing is a typically nonlinear free-surface flow, with a large deformation. Accurate free surface tracking is the focus (and difficulty) of the numerical simulation. Volume of Fluid (VOF) [32] and Level-set [33] are popular mathematical models for detecting free surface in Euler mesh methods. In recent years, meshless particle methods have become increasingly popular for simulating violent free-surface flows, thanks to their inherent advantage in recognizing free surfaces [34–36]. The famous meshless particle methods include Smoothed Particle Hydrodynamics (SPH) [37,38] and the Moving Particle Semi-implicit (MPS) method [39]. Delorme et al. [40] used SPH method to investigate the impact pressure in shallow water sloshing. Zhang et al. [41] investigated the Faraday wave phenomenon in a square tank using MPS method, as well as analyzing the mechanism of resonance response. Sanchez-Mondragon et al. [42] studied the sloshing of a prismatic LNG tank with vertical baffles, comparing the influence of having no baffle, a single baffle, and two baffles on sloshing suppression. Wang et al. [43] studied liquid sloshing with vertical baffles under rotation excitation, using an improved MPS method.

Based on the improved MPS method (BM-MPS) proposed by Wang et al. [44], the two-dimensional liquid sloshing with vertical slotted screens under rotation excitation has also been investigated in this study; additionally, the damping effect and mechanism of vertical-slotted screens has been explored. By improving the pressure Poisson equation source term and the pressure gradient discrete model, the BM-MPS method had significant advantages on the impact pressure calculation, in addition to having first-order convergence in space [44]. In accordance with the impact pressure results of the physical experiment reported by Delorme [40], the accuracy of our calculated results was first verified to prove the reliability of the numerical model. Afterward, the damping effect and mechanism of the vertical-slotted screen has been discussed in detail. This analysis included the influence of the porosity on an examination of the impact pressure and resonance period as influenced by the porosity, as well as an assessment of the impact of rotation amplitude.

2. BM-MPS Method

2.1. Governing Equations

In the MPS method, the governing equations of the motion of fluid flows are the Lagrangian continuity and Navier–Stokes equations, which can be expressed as follows [39]:

$$\frac{1}{\rho}\frac{D\rho}{Dt} + \nabla \cdot \boldsymbol{u} = 0, \tag{1}$$

$$\frac{D\boldsymbol{u}}{Dt} = -\frac{1}{\rho}\nabla p + \nu\nabla^2\boldsymbol{u} + \boldsymbol{g}, \tag{2}$$

where $\boldsymbol{u}$ is the velocity vector, t is the time, ρ is the density of the fluid, p is the pressure, ν is the kinematic viscosity coefficient, and $\boldsymbol{g}$ is the gravitational acceleration. For an incompressible fluid, the derivative of density with respect to time ($D\rho/Dt$) is zero.

2.2. Operator Discretization

In the original MPS method, the Gradient, Laplacian, and divergence operators are generally discretized as follows [39]:

$$< \nabla\phi >_i = \frac{D_s}{n_0}\sum_{j\neq i}\frac{\phi_j - \phi_i}{r_{ij}^2}(r_j - r_i)w_{ij} \tag{3}$$

$$< \nabla^2\phi >_i = \frac{2D_s}{n_0\lambda}\sum_{j\neq i}(\phi_j - \phi_i)w_{ij}, \lambda = \frac{\sum\limits_{j\neq i} r_{ij}^2 w_{ij}}{\sum\limits_{j\neq i} w_{ij}} \tag{4}$$

$$< \nabla\phi >_i = \frac{D_s}{n_0}\sum_{j\neq i}\frac{(\phi_j - \phi_i)\cdot(r_j - r_i)}{r_{ij}^2}w_{ij} \tag{5}$$

where, D_s is the spatial dimension, n_0 is the initial particle number density, w represents kernel function, r is the coordinate vector of a particle, r_{ij} denotes the distance between particles I and j, $r_{ij} = |r_j - r_i|$. In theory, the target particle i will interact with other particles in the entire computational domain. In order to reduce computing cost, the effective range of the kernel function (namely, the radius of the influence domain r_e) is generally given. In this study, the standard kernel function proposed by Koshizuka and Oka [39] was used as the kernel function:

$$w(r_{ij}) = \begin{cases} \frac{r_e}{r_{ij}} - 1 & , \quad 0 < r_{ij}/r_e < 1 \\ 0 & , \quad r_{ij}/r_e \geq 1 \end{cases} \tag{6}$$

where r_e is set as 2.4 l_0, and l_0 symbolizes the initial particle space distance.

2.3. Pressure Poisson Equation

According to the Helmholtz–Hodge decomposition principle, the MPS method is a semi-implicit two-step algorithm for calculating the momentum equation (Equation (2)). During this process, a pressure Poisson equation can be derived for updating the pressure field.

The source term of the pressure Poisson equation has significant influence on the calculation accuracy of pressure. The original, proposed by Koshizuka et al. [39], can effectively prevent the clustering of particles well, but it is liable to cause numerical pressure oscillation.

In this study, a modified source term was adopted, on the basis of the research achievements of Khayyer et al. [45] and Tanaka [46], which can be expressed as [47]:

$$-\frac{\Delta t}{\rho_0}\nabla^2 p_i^{k+1} = -(1-\gamma)\frac{1}{n_0}\sum_{j\neq i}\left(\frac{r_e}{r_{ij}^3}(\boldsymbol{u}_j-\boldsymbol{u}_i)\cdot(\boldsymbol{r}_j-\boldsymbol{r}_i)\right)^* + \frac{1}{n_0}\gamma\frac{n_i^*-n_0}{\Delta t} \tag{7}$$

where the principal part of the source terms is the velocity divergence. To guarantee the conservation of fluid volume, the derivative of particle number density with time was also considered. Herein, * indicates an intermediate result at each calculation time step. γ is the ratio coefficient, ranging from 0.001 to 0.05, with 0.01 being recommended.

As for the velocity divergence term in Equation (7), the Background Mesh scheme (BM) [44] was incorporated for its calculation. The size of the background mesh is kept consistent with the particle size. The value of the velocity divergence was first calculated based on the nodes of background mesh, before then being interpolated onto discrete particles. As for the detailed explanation for the BM scheme, please refer to Wang et al. [44].

2.4. Pressure Gradient Model

The pressure gradient model is an important factor affecting the calculation of pressure and the energy conservation [48,49]. In order to reduce the numerical energy dissipation in the simulation, the pressure gradient model (obtained based on a Taylor series expansion) is adopted, which has first-order accuracy [47]:

$$\langle\nabla p\rangle_i = \begin{cases} C_i^{-1}\left[\frac{1}{n_0}\sum\limits_{i\neq j}\frac{p_j-\hat{p}_i}{r_{ij}^2}(\boldsymbol{r}_j-\boldsymbol{r}_i)w(r_{ij},r_e)\right] & , \ |C_i|\geq\alpha_c \\ \frac{D_s}{n_0}\sum\limits_{i\neq j}\frac{p_j-\hat{p}_i}{r_{ij}^2}(\boldsymbol{r}_j-\boldsymbol{r}_i)w(r_{ij},r_e) & , \ |C_i|<\alpha_c \end{cases} \tag{8}$$

$$C_i = \left[\frac{1}{n_0}\sum_{i\neq j}w(r_{ij},r_e)\frac{(\boldsymbol{r}_j-\boldsymbol{r}_i)}{r_{ij}}\otimes\frac{(\boldsymbol{r}_j-\boldsymbol{r}_i)^T}{r_{ij}}\right] \tag{9}$$

Considering the special case that C_i has not been inversed due to particle splashing, the new model combines the original pressure Gradient model; thus, it is referred to as the Combined pressure Gradient Model (CGM). The value of coefficient α_c was recommended as 0.005.

2.5. Boundary Conditions

In MPS method, the basic boundary conditions include free surface boundary conditions and solid wall boundary conditions. Dynamic boundary conditions have been implemented for the free surface boundary. As for the recognition of free surface, the criteria for identifying free surface particles were as follows:

$$\begin{aligned} & n_i < \beta n_0 \\ & A_i < \alpha A_0\ ,\ A_i = \sum_{j\neq i}\frac{|\boldsymbol{r}_j-\boldsymbol{r}_i|}{l_0}w(r_{ij}) \end{aligned} \tag{10}$$

where A_i symbolizes the filling rate (the percentage of the influence domain of target particle i covered by its surrounding particles), and A_0 is the filling rate of inner particles at the initial moment. The value of α and β was chosen as 0.88 and 0.97, respectively.

For the solid wall boundary, no-slip boundary conditions are usually used. A solid wall boundary consists of wall particles and dummy particles. For wall particles, the physical properties were consistent with those of fluid particles, participating in the calculation of the pressure Poisson equation. Dummy particles only took part in the calculation of the particle number density.

3. Numerical Model

The settings of numerical liquid tank are shown in Figure 1, which are in accordance with the conditions of the physical experiment presented by Delorme et al. [40]. The tank was 0.9 m long, 0.58 m high, and had an initial water depth of 0.093 m. The center of rotation was at point O on the midperpendicular of the tank, at a distance of 0.184 m from the bottom boundary. The tank was forced with a sinusoidal rotation motion as:

$$\theta = -\theta_{\max} \sin \omega t \tag{11}$$

where $\theta_{\max}$ is the maximum angle of rotation and the default is the experimental value of 0.07 rad. ω denotes the excitation frequency, which was calculated as $\omega = 2\pi/T_E$, where T_E is the excitation period.

Two pressure calculation points (A and B) were set at the intersections of the still water surface and the lateral borders, as shown in Figure 1. The fluid density and kinematic viscosity coefficient were set according to the physical properties of water, which were $\rho = 1000\ \text{kg/m}^3$ and $v = 10^{-6}\ \text{m}^2/\text{s}$, respectively. A vertical slotted screen was positioned in the center of the tank, as depicted in Figure 1, with S_g representing the slot size, which had a default value of $3l_0$. The porosity of the slotted screen, ε was defined as:

$$\varepsilon = S_g/S_c \tag{12}$$

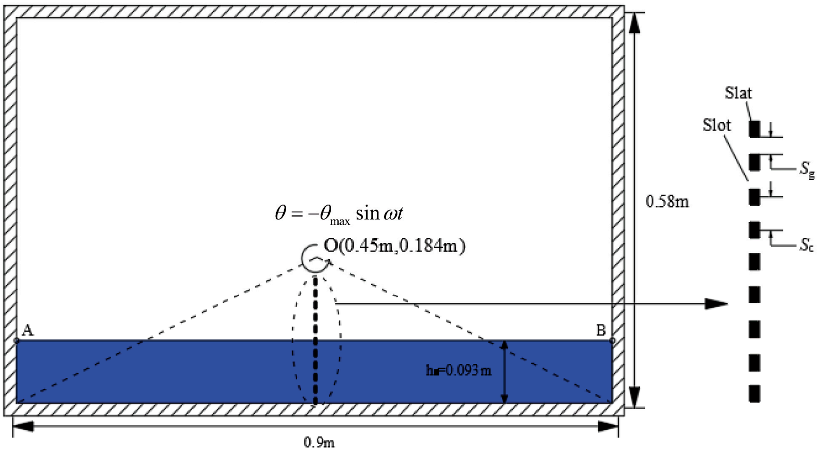

Figure 1. Schematic diagram of the initial calculation conditions.

According to the linear analytical solution reported by Faltinsen [21], the intrinsic frequency could be calculated from the following equation:

$$\omega_n^2 = g\frac{(2n+1)\pi}{L}\tanh\left\{\frac{(2n+1)\pi}{L}h\right\},\ T = \frac{2\pi}{\omega_n}, \tag{13}$$

where L is the length of the tank, h is the water depth, and n is the modulus. In this study, the first natural frequency was $\omega_0 = 3.277\ \text{s}^{-1}$, corresponding to the period $T_0 = 1.917$ s.

Due to the condition of this study being a two-dimensional excitation, the main movement of the water particle was along the x and z axes. As such, the motion states in two and three dimensions were very similar. Hence, a two-dimensional numerical model was built for the following research.

In order to verify the validity of numerical simulation results, the liquid sloshing motion under a two-dimensional rotation excitation without a baffle was simulated based on the present numerical model, the results of which were compared with the experimental results of Delorme et al. [40]. The excitation period was set as the resonance period (T_R) of the condition of the sloshing without baffle, $T_E = 1.91$ s, and the particle size l_0 was chosen as 0.003 m. Figure 2a compares the impact pressure at point A, calculated using the

BM-MPS numerical model with the experimental results, using a dimensionless pressure magnitude. Figure 2b focuses on the third and fourth peaks, as indicated in Figure 2a. The comparison result shows that the diachronic variation and maximum peak value were in good agreement with the experimental results. This demonstrated that the numerical model used in this study was accurate enough to meet the requirements of subsequent research. Additionally, Figure 2 presents the calculated impact pressure when a vertical slotted screen was placed in the middle of the tank. It is evident that there was a noticeable decrease in impact pressure at point A.

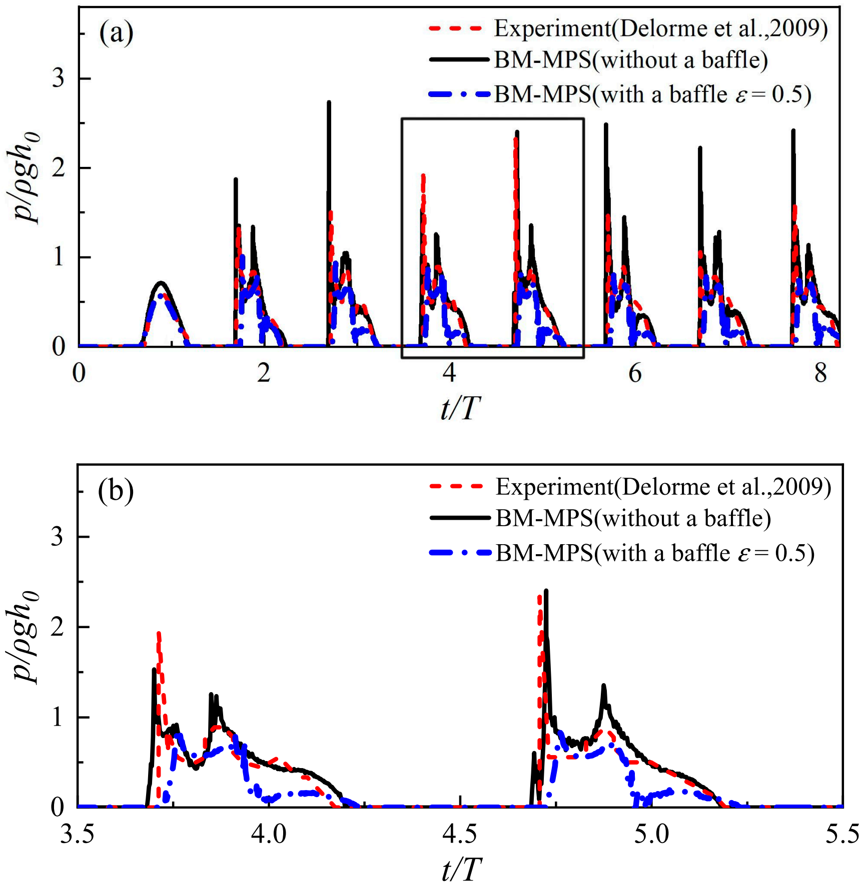

Figure 2. Comparisons between the numerical and experimental results [40].

Figure 3 shows the snapshots of sloshing motion both in the tank without and in the tank with a vertical-slotted screen (ε = 0.5), simulated using the BM-MPS method under the excitation period T_E = 1.91 s. The simulated surface patterns without a baffle had a good agreement with the corresponding experimental ones. Moreover, a clear contrast could be observed between the images with and without the slotted screen, indicating that the presence of the vertical-slotted screen had a substantial effect on sloshing suppression.

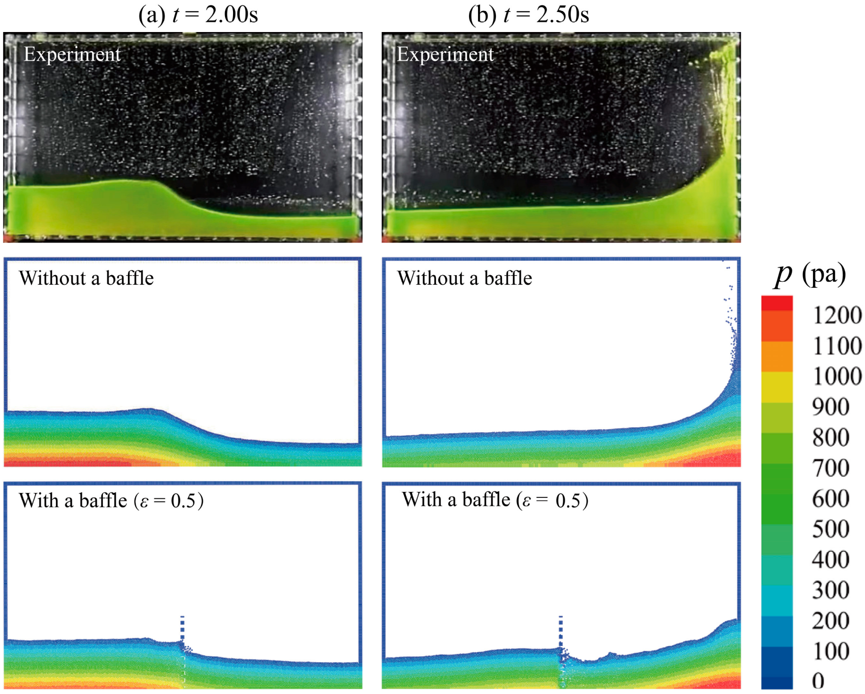

Figure 3. Snapshots of sloshing flow with pressure field under the excitation period T_E = 1.91 s. (**a**) t = 2.00 s; (**b**) t = 2.50 s.

4. Result and Discussion

4.1. The Effect of Porosity on Impact Pressure

Figure 4 shows the time variation curve of the impact pressure at point A for the vertical-slotted screens with different porosities. The excitation period remained fixed at 1.91 s. Figure 4a compares the impact pressure waveforms for porosities ranging from 0 to 0.3. The results revealed that the maximum impact pressure increased as the porosity increased. When the porosity was small, the pressure curve appeared as a mound shape. When the porosity reached 0.3, the mean value of $p/\rho gh$ was about 0.531, and the pressure curve exhibited distinct single peaks. Figure 4b corresponds to the outcomes for the porosity values, ranging from 0.375 to 0.6. When the porosity was 0.375, the pressure variation curve showed a double peak phenomenon, where the first peak was slightly smaller than the second. As for the porosities where ε = 0.43, 0.5, and 0.6, the mean of the peak pressure continued to increase as the porosity increased, and the shape of the double-peak changed. When the porosity was 0.43, both the peaks in the bimodal phenomenon were similar in size. However, when the porosity reached 0.5, the first of the double peaks became larger than the second. When the porosity increased to 0.6, the pressure curve was quite similar to the one without a baffle. At this point, the mean of the peak pressure rose to 1.382, which was significantly less than the sloshing without a baffle, but significantly larger than that where ε = 0.5.

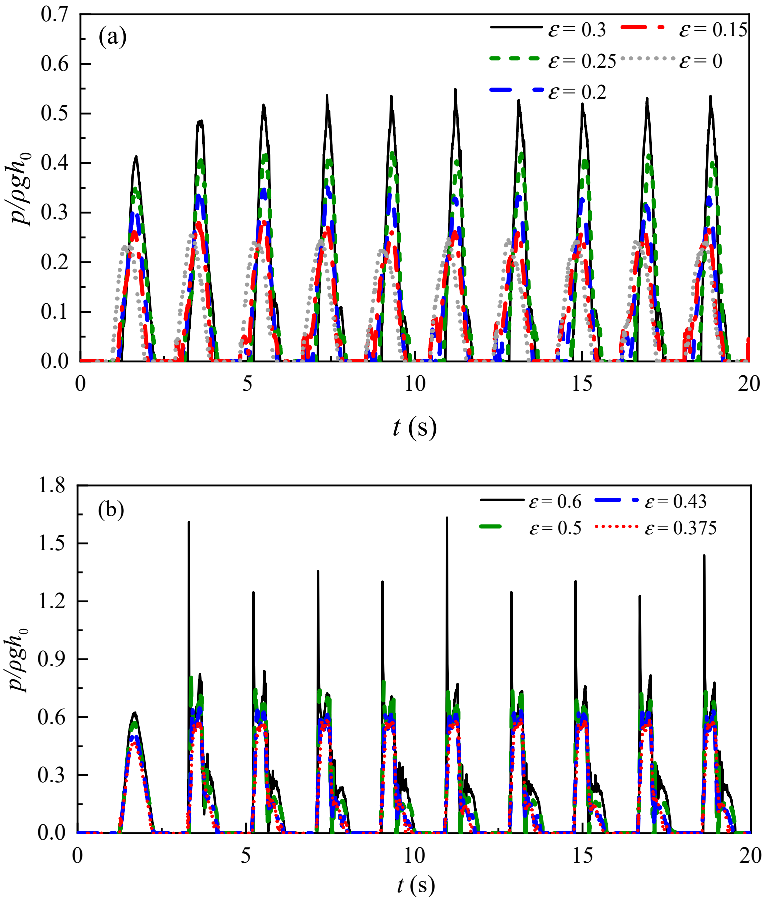

Figure 4. The time histories of calculated pressure at point A under different porosities (T_E = 1.91 s). (**a**) ε = 0, 0.15, 0.2, 0.25, 0.3; (**b**) ε = 0.375, 0.43, 0.5, 0.6.

4.2. The Effect of Slot Size on Impact Pressure

Figure 5 shows the time-variation curves of impact pressure at the left and right junction points of the water surface and the wall, with the slot sizes of $2l_0$, $3l_0$, and $4l_0$ for ε = 0.5. Figure 5a represents the calculated result of point A. The pressure variation curves exhibited similar patterns across the three different slot sizes, all showing obvious double peak phenomena. However, the first pressure peak was increased as the slot size became larger. Figure 5b shows the impact pressure curves at point B, which exhibited a double peak phenomenon similar to that observed at point A. The maximum pressure at point B was slightly lower than that at point A, and the values of the two peaks were similar in their double peak phenomenon. These findings indicated that the sloshing suppression effect of the slotted screen was more pronounced with decreased slot sizes, given the same porosity conditions.

To provide further clarification on the variation characteristics of maximum impact pressure, the maximum value of each pressure pattern was extracted, as displayed in Figure 6. Each solid line represented the average of the corresponding group. As shown in Figure 6a, the magnitude and fluctuation of the pressure were both largest when $S_g = 4l_0$. The trend of the maximum pressure change with the slot size was similar at point B. However, the difference was smaller and more stable than that at point A. Figure 7 shows the distribution of the valid value ($p_{1/3}$) of each impact pressure pattern and its mean value for different slot sizes. The valid value was determined by calculating the average of the highest third of the pressure values. Each set of values was subjected to the exclusion of the maximum and minimum values prior to being averaged, thereby rendering the resulting averages more reliable. Similar to Figure 6, the larger the aperture, the larger the corresponding value, though the deviation was significantly smaller. Otherwise, the valid values at points A and B were of similar magnitude, and their mean values were likewise very close. Table 1 gives the analysis result of the relative error and root-mean-square error (RMSE).

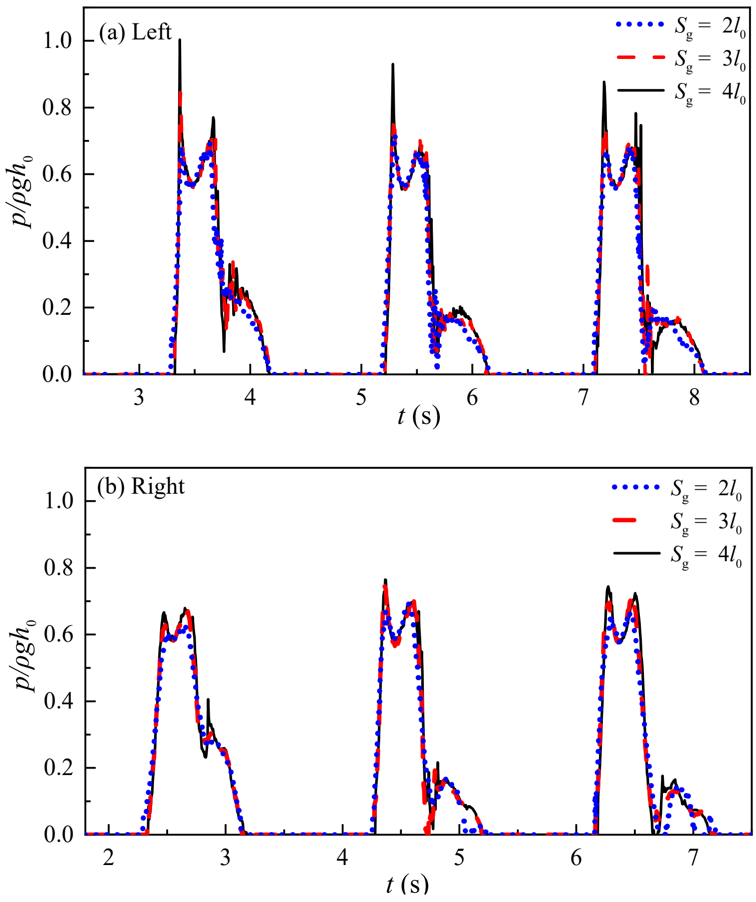

Figure 5. Impact pressure curves for different slot sizes where ε = 0.5. (**a**) The impact pressure of point A on the left; (**b**) The impact pressure of point B in the right.

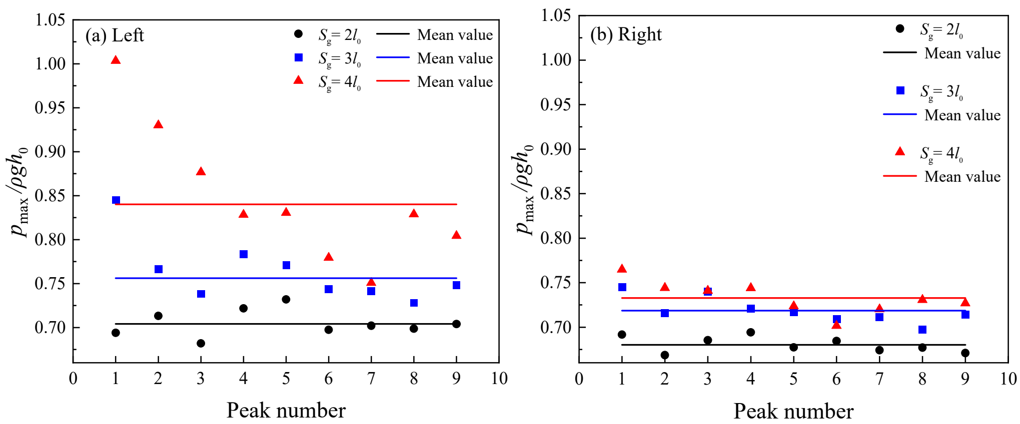

Figure 6. The distributions of maximum impact pressure p_{max} at points A and B for different slot sizes. (**a**) The impact pressure of point A on the left; (**b**) The impact pressure of point B in the right.

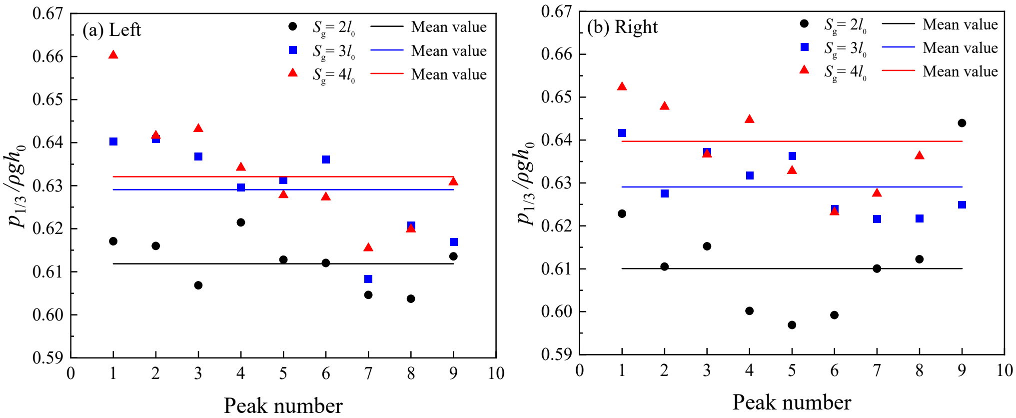

Figure 7. The distributions of the valid value $p_{1/3}$ at points A and B, under different pore sizes. (**a**) The impact pressure of point A on the left; (**b**) The impact pressure of point B in the right.

Table 1. The analysis result of the relative error and root-mean-square error.

NUM	S_g											
	$2l_0$				$3l_0$				$4l_0$			
	p_{max}	δ	$p_{1/3}$	δ	p_{max}	δ	$p_{1/3}$	δ	p_{max}	δ	$p_{1/3}$	δ
1	0.694	1.57%	0.692	1.66%	0.845	10.76%	0.745	3.61%	1.003	18.32%	0.765	4.34%
2	0.713	1.17%	0.669	1.74%	0.767	0.50%	0.716	0.46%	0.930	9.68%	0.744	1.53%
3	0.682	3.27%	0.685	0.73%	0.738	3.24%	0.740	2.90%	0.877	3.38%	0.741	1.09%
4	0.722	2.39%	0.694	2.03%	0.784	2.73%	0.721	0.30%	0.828	2.33%	0.744	1.51%
5	0.732	3.82%	0.677	0.46%	0.771	1.09%	0.717	0.26%	0.830	2.07%	0.724	1.28%
6	0.697	1.07%	0.685	0.60%	0.744	2.54%	0.709	1.38%	0.779	8.09%	0.702	4.28%
7	0.702	0.42%	0.674	0.92%	0.742	2.79%	0.712	1.05%	0.751	11.46%	0.720	1.75%
8	0.699	0.91%	0.677	0.50%	0.728	4.59%	0.698	2.98%	0.829	2.26%	0.731	0.31%
9	0.704	0.14%	0.671	1.39%	0.748	1.93%	0.714	0.67%	0.804	5.16%	0.727	0.83%
Mean value	0.704	/	0.680	/	0.756	/	0.718	/	0.84	/	0.733	/
RMSE(σ)	0.015	/	0.008	/	0.033	/	0.013	/	0.076	/	0.018	/

Note: δ is the relative error, and the calculation formula is $\delta = \frac{|p-\overline{p}|}{\overline{p}}$.

4.3. The Effect of Slotted Screen on the Resonance Period

The calculation formula of intrinsic frequency (Equation (13)) is mainly appropriate for the liquid sloshing in a 2D rectangular tank without any damping structures. The existence of a slotted screen will more or less affect the resonance characteristics of liquid sloshing. The effect of porosities and slot sizes on the resonance characteristics is discussed in Figure 8 by analyzing the impact pressure at point A. Figure 8a shows the variation curve of the maximum impact pressure with different excitation periods under different porosity conditions, considering the cases where ε = 0, 0.1, 0.15, 0.2, 0.25, 0.375, and 0.5, respectively. When ε = 0.5, a distinct peak occurred around the excitation period of 1.8 s, indicating a resonance period around 1.8 s at this condition. When ε = 0.375, the resonance period occurred at T_E = 1.91 s, which is consistent with that of the unbaffled state. The resonance period was roughly 2.0 s when the porosity was 0.25 and 0.2. As for ε = 0.5 to 0.2, the resonance periods basically occurred around the intrinsic frequency of no-baffle sloshing. However, different phenomenon appeared when ε = 0.15. A second peak occurred at T_E = 1.1 s, although the resonance period was still around 2.0 s. When the porosity decreased to 0.1, the resonance period changed significantly, with the peak impact pressure occurring at T_E = 1.1 s, identical to the resonance period of the nonporous baffle (ε = 0).

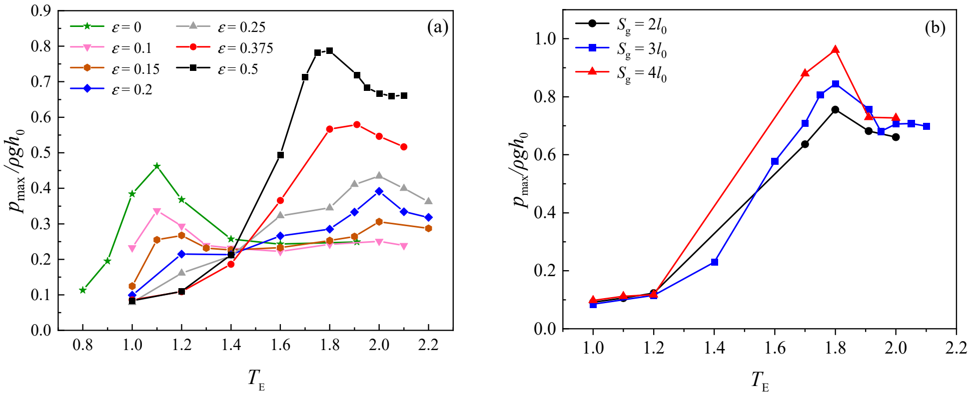

Figure 8. Variations of average maximum pressure with excitation period for different porosities and pore sizes. (**a**) The variation curve of the maximum impact pressure with different excitation periods for different porosities; (**b**) The maximum impact pressure response to different excitation periods for different slot sizes at $\varepsilon = 0.5$.

Figure 8b shows the maximum impact pressure response to different excitation periods for different slot sizes at $\varepsilon = 0.5$, considering the cases where $S_g = 2l_0$, $3l_0$, and $4l_0$, respectively. The results show the resonance periods were all around 1.8 s, which indicated that the slot size did not affect the resonance phenomenon.

Figure 9 shows the correlation between the porosity and the maximum impact pressure in resonance, as well as the relationship between the porosity and the resonance period. The *y*-axis on the left side represents the maximum impact pressure, whereas the *y*-axis on the right side represents the resonant period. There was an interesting phenomenon in that the turning point of resonance period occurred at $\varepsilon = 0.1$, but the maximum impact pressure was not the minimum. When the porosity of the slotted screen was 0.15, the maximum impact pressure in resonance was at its minimum. As the porosity increased or decreased, the maximum impact pressure tended to rise.

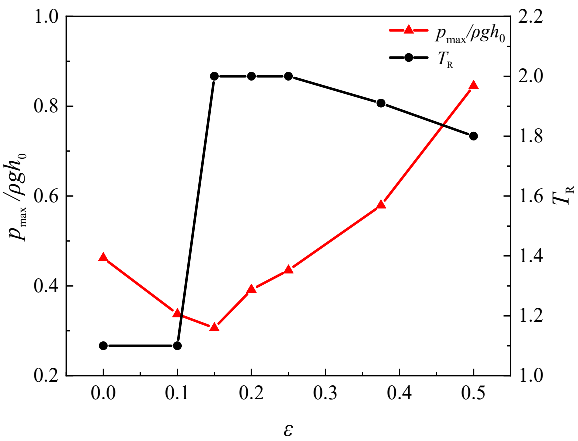

Figure 9. Average maximum impact pressure at point A with different porosities at the state of resonance.

Fluid energy dissipation in the form of vortex damping is a one of the important mechanisms for suppressing sloshing, especially for porous baffles. Figure 10 shows the variation curves of the positive and negative rot$\boldsymbol{u}$ under excitation of the resonance period for different porosities. The value of rot$\boldsymbol{u}$ is an important parameter to reflect the intensity of vortex. The positive and negative vortices were basically symmetrical. When the porosity was small, the vortex effect was remarkable. The average maximum and valid values of the positive and negative rot$\boldsymbol{u}$ were calculated and have been listed in Table 2. When the porosity was around 0.15, 0.2 and 0.25, the turbulence intensity was obviously greater than that of other porosities, which indicated that the slotted screen produced a better damping effect when its porosity was in the range of 0.15 to 0.25. The turbulence intensity reached its maximum when ε = 0.15, which corresponds to the minimum pressure point in Figure 9. Furthermore, at a porosity of 0.5, the curl was considerably reduced, suggesting the prevalence of only minor eddies under highly porous conditions.

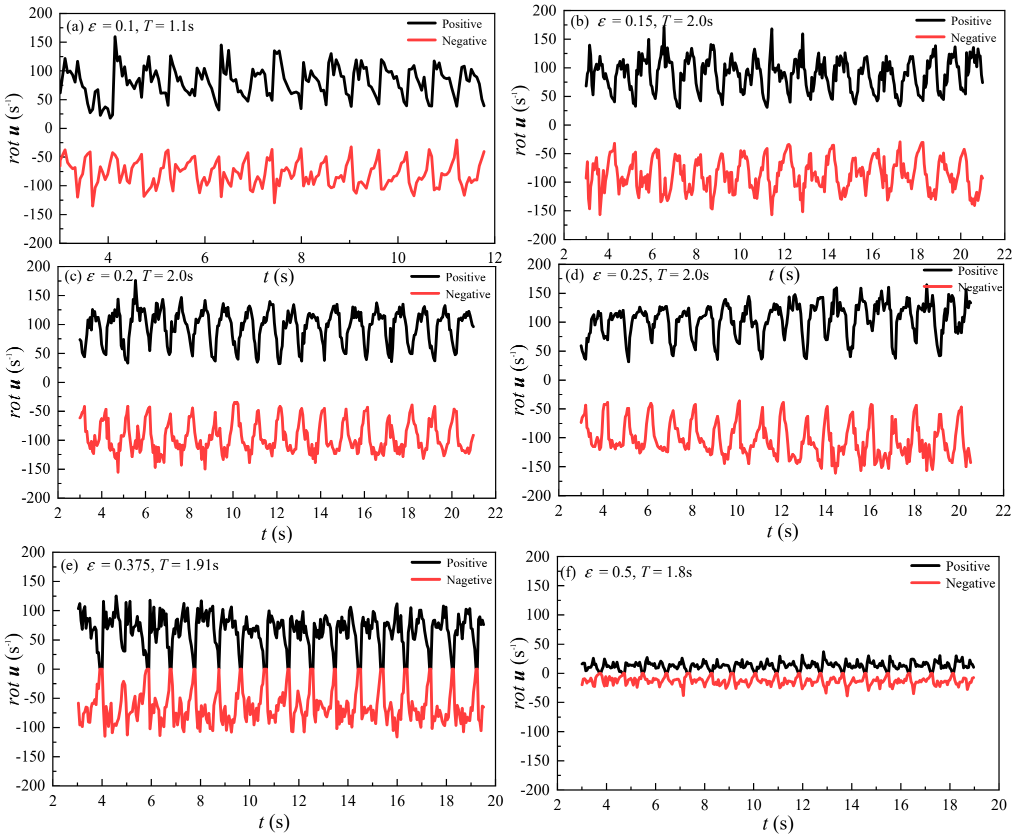

Figure 10. Time histories of rot***u*** for different porosities.

Table 2. The average maximum and valid values of the positive and negative rot***u*** for different porosities. (unit: s^{-1}).

	e											
	0.1		**0.15**		**0.2**		**0.25**		**0.375**		**0.5**	
	(rot)$_+$	**(rot)$_-$**	**(rot)$_+$**	**(rot)$_-$**	**(rot)$_+$**	**(rot)$_-$**	**(rot)$_+$**	**(rot)$_-$**	**(rot)$_+$**	**(rot)$_-$**	**(rot)$_+$**	**(rot)$_-$**
Mean value	134.6	−119.3	148	−144.9	145.7	−141.9	136.4	−135.2	115	−110.4	29.7	−30.9
Valid value	110.4	−102.6	119.2	−118.4	114.6	−117.9	112.2	−112.3	93.7	−92.1	20.1	−20.2

4.4. The Effect of Rotation Amplitude on Impact Pressure

Figure 11 shows the correlation between the maximum impact pressure and the rotation amplitude, considering the maximum rotation angle θ_{max} = 0.02, 0.03, 0.05, 0.07, and 0.09 rad. The porosity of these cases was 0.5, and the excitation periods were 1.7 s, 1.8 s, and 1.9 s, respectively. The linear relationship between the rotation amplitude and the maximum impact pressure was clear, regardless of the different excitation periods, and the correlation coefficients were larger than 0.99. When the rotation amplitudes were less than 0.04 rad, the resonance period was consistent with those of the case of no-baffle sloshing. This indicated that the alteration in the resonance characteristic of sloshing was dependent on the amplitude of excitation. Furthermore, the slopes of the two fitted curves were very close when the excitation period were 1.7 s and 1.8 s. However, for an excitation period of T_E = 1.9 s, the slope decreased markedly, due to the change in resonance period.

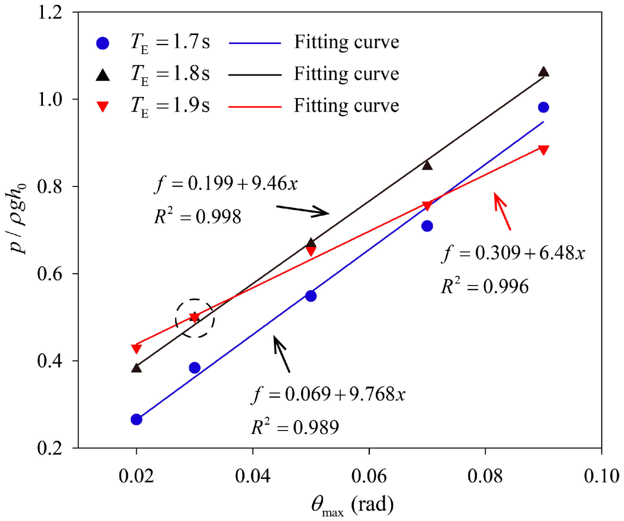

Figure 11. Correlation between the maximum impact pressure and rotational angle.

Figure 12 presents the patterns of the impact pressure for different rotation amplitudes where T_E = 1.8 s. When the amplitude was 0.02 rad or 0.03 rad, the pressure at point A was small, and the curve displayed a hump shape, without a distinct peak. When the amplitude was equal to or greater than 0.05 rad, the double peak phenomenon appeared on the graph. The maximum of each pressure wave-form at points A and B was extracted in Figure 13, under the conditions of different excitation amplitudes. The result of Figure 13b was similar to that of Figure 13a. As the excitation amplitude increased, the uniformity of the maximum impact pressure decreased.

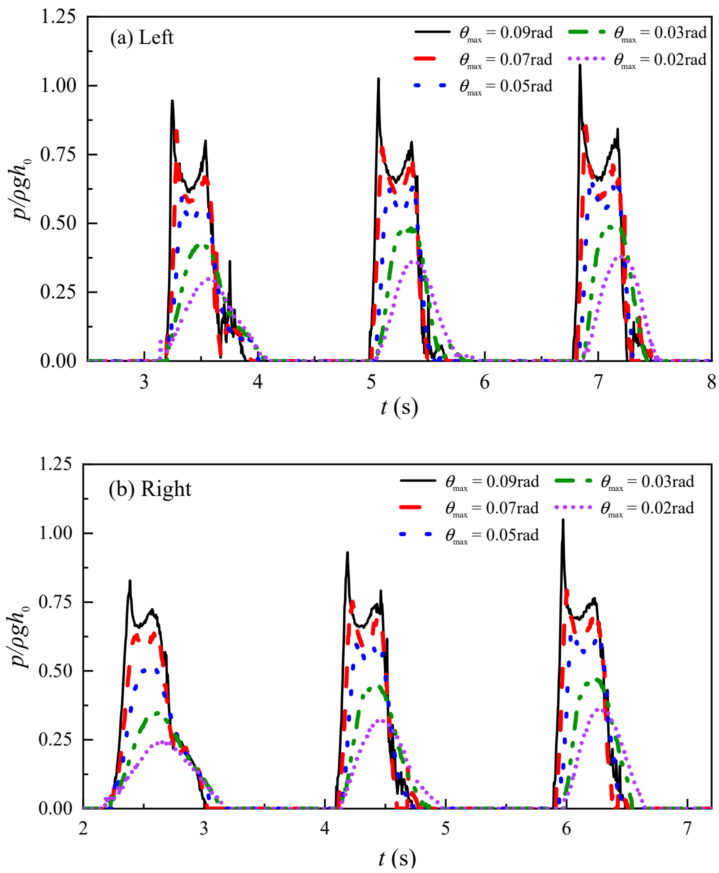

Figure 12. Waveforms of impact pressure under rotational angles (T_E = 1.8 s).

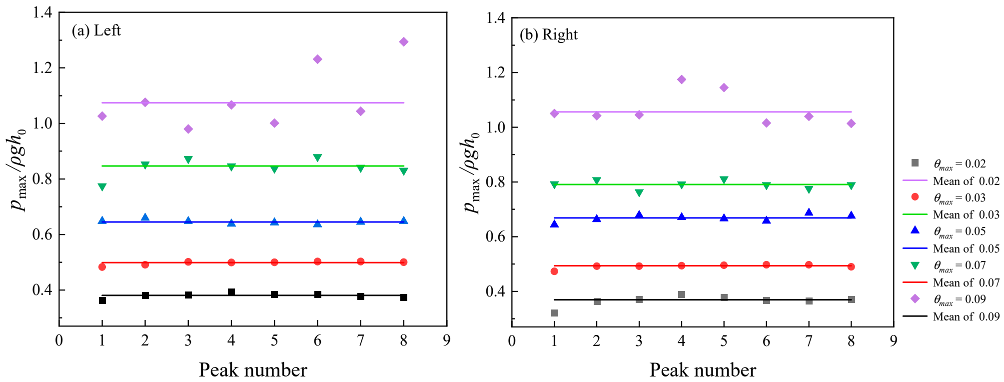

Figure 13. Distributions of the first peak, and mean values at point A and point B for different rotation amplitudes.

5. Conclusions

This study was based on the BM-MPS method to simulate the liquid sloshing motion with a vertical slotted screen under rotation excitation conditions. By analyzing the effect of porosity and rotation amplitude on the impact pressure, the effect and mechanism of the vertical slotted screen on sloshing suppression was investigated, and the following points can be summarized:

1. The porosity was a crucial parameter that determined the damping effect of the slotted screen. Generally, the maximum impact pressure increased as the porosity increased. Meanwhile, with the decrease in the damping effect, the pattern of impact pressure changed from a mounded structure to a single peak structure, and then to a double peak structure, and the first peak became more and more prominent.
2. The resonance characteristic of liquid sloshing with a vertical-slotted screen was bound up with the porosity. When the porosity was 0.1 or smaller, resonance was observed at around T_E = 1.1 s. When the porosity was large, the resonance period was in the range of 1.8 to 2.0, varying around the period corresponding to the first natural frequency in the unbaffled condition. In addition, the decrease in the maximum impact pressure in resonance was not always consistent with the decrease in the porosity. The porosity of 0.15 was where the maximum impact pressure reached its minimum point, thereby achieving the most significant attenuation of sloshing. At this moment, the intensity of the vortex was at its largest. As for slotted screens, the combined effect of hydrodynamic damping and vortex damping had a better performance in sloshing suppression. This porosity is thus recommended for practical engineering applications.
3. The size of the slot has a less significant effect on the impact pressure. When the porosity was the same but the slot size enlarged, the maximum impact pressure increased slightly. Nonetheless, the dissimilarity between the maximum impact pressure and pressure waveform was negligible.
4. The rotation amplitude was a factor that affected the resonance period. As the amplitude increased, the resonance period changed from 1.91 s to 1.8 s. In addition, the maximum impact pressure increased as the maximum rotation angle increased.

Author Contributions: Investigation, writing and editing, data analysis, and formal analysis, C.Z.; conceptualization, methodology, editing, funding acquisition, L.W.; supervision and project administration, M.X. All authors have read and agreed to the published version of the manuscript.

Funding: This study is financed by Natural Science Foundation of Jiangsu Province (BK20200729), the National Natural Science Foundation of China (42206168), and The Belt and Road Special Foundation of the State Key Laboratory of Hydrology-Water Resources and Hydraulic Engineering (2021nkms05).

Institutional Review Board Statement: Not applicable.

Informed Consent Statement: Not applicable.

Data Availability Statement: Not applicable.

Conflicts of Interest: The authors declare no conflict of interest.

References

1. Park, J.J.; Kim, S.Y.; Kim, Y.; Seo, J.-H.; Jin, C.H.; Joh, K.H. Study on tank shape for sloshing assessment of LNG vessels under unrestricted filling operation. *J. Mar. Sci. Technol.* **2015**, *20*, 640–651. [CrossRef]
2. Yu, L.; Xue, M.; Zhu, A. Numerical Investigation of Sloshing in Rectangular Tank with Permeable Baffle. *J. Mar. Sci. Eng.* **2020**, *8*, 671. [CrossRef]
3. Golla, S.T.; Venkatesham, B. Experimental study on the effect of centrally positioned vertical baffles on sloshing noise in a rectangular tank. *Appl. Acoust.* **2021**, *176*, 107890. [CrossRef]
4. Ju, H.B.; Jang, B.S.; Ki-Ho, Y. Prediction of sloshing pressure and structural response of LNG CCS. *Ocean Eng.* **2022**, *266*, 112298. [CrossRef]
5. Goudarzi, M.A.; Farshadmanesh, P. Numerical evaluation of hydrodynamic damping due to the Upper Mounted Baffles in real scale tanks. *Soil Dyn. Earthq. Eng.* **2015**, *77*, 290–298. [CrossRef]
6. Uemichi, A.; Takai, A.; Sakai, H.; Kaneko, S.; Yamasaki, Y. Sloshing in a Horizontal Cylindrical Tank Subjected to Pitching Excitation and Damping Effects by Perforated Plates. *J. Press. Vessel Technol.* **2017**, *139*, 041302. [CrossRef]
7. Arif, U.G.M.; Loo, C.T.; Kang, H.S.; Punurai, W.; Quen, L.K.; Lai, G.N.Y. Suppression of hydrodynamic sloshing in liquefied natural gas tank with floating baffle: Experimental and numerical studies. *IOP Conf. Ser. Earth Environ. Sci.* **2020**, *463*, 012111. [CrossRef]
8. Nimisha, P.; Jayalekshmi, B.R.; Venkataramana, K. Slosh damping in rectangular liquid tank with additional blockage effects under pitch excitation. *J. Fluids Eng.* **2022**, *144*, 121403. [CrossRef]
9. Jin, X.; Liu, M.; Zou, Y.; Luo, M.; Yang, F.; Wang, L. Numerical simulation of Faraday waves in a rectangular tank and damping mechanism of internal baffles. *J. Fluids Struct.* **2022**, *109*, 103503. [CrossRef]
10. Celebi, M.S.; Akyildiz, H. Nonlinear modeling of liquid sloshing in a moving rectangular tank. *Ocean Eng.* **2002**, *29*, 1527–1553. [CrossRef]
11. Akyildız, H.; Ünal, N.E. Sloshing in a three-dimensional rectangular tank: Numerical simulation and experimental validation. *Ocean Eng.* **2005**, *33*, 2135–2149. [CrossRef]
12. Liu, D.; Lin, P. Three-dimensional liquid sloshing in a tank with baffles. *Ocean Eng.* **2008**, *36*, 202–212. [CrossRef]
13. Jiang, S.; Bai, W.; Lan, J. Influence of a vertical baffle on suppressing sway motion response of a tank coupled with sloshing actions in waves. *Ocean Eng.* **2022**, *260*, 111999. [CrossRef]
14. Yao, W.; Li, J.; Mu, C.; Hui, H.; Hua, T.J. Numerical and experimental analysis of the effect of elastic membrane on liquid sloshing in partially filled tank vehicles. *Mech. Based Des. Struct. Mach.* **2023**, *51*, 1741–1757. [CrossRef]
15. Shao, J.; Li, S.; Li, Z.; Liu, M. A comparative study of different baffles on mitigating liquid sloshing in a rectangular tank due to a horizontal excitation. *Eng. Comput.* **2015**, *32*, 1172–1190. [CrossRef]
16. Xavier, V.R.; Ehsan, S.; Ibuki, K.; Andrés Amador, G. Study of the Sloshing Dynamics in Partially Filled Rectangular Tanks with Submerged Baffles Using VOF and LES Turbulence Methods for Different Impact Angles. *Computation* **2022**, *10*, 225. [CrossRef]
17. Jin, H.; Liu, Y.; Li, H. Experimental study on sloshing in a tank with an inner horizontal perforated plate. *Ocean Eng.* **2014**, *82*, 75–84. [CrossRef]
18. Cho, I.H.; Kim, M.H. Effect of dual vertical porous baffles on sloshing reduction in a swaying rectangular tank. *Ocean Eng.* **2016**, *126*, 364–373. [CrossRef]
19. Zang, Q.; Fang, H.; Liu, J.; Lin, J. Boundary element model for investigation of the effects of various porous baffles on liquid sloshing in the two dimensional rectangular tank. *Eng. Anal. Bound. Elem.* **2019**, *108*, 484–500. [CrossRef]
20. Mahamad, A.A.; Mohamed, A.M. A Numerical Study on the Effects of Perforated and Imperforate Baffles on the Sloshing Pressure of a Rectangular Tank. *J. Mar. Sci. Eng.* **2022**, *10*, 1335. [CrossRef]
21. Faltinsen, O.M.; Timokha, A.N. Natural sloshing frequencies and modes in a rectangular tank with a slat-type screen. *J. Sound Vib.* **2010**, *330*, 1490–1503. [CrossRef]
22. Xue, M.; Lin, P.; Zheng, J.; Ma, Y.; Yuan, X.; Nguyen, V.T. Effects of perforated baffle on reducing sloshing in rectangular tank: Experimental and numerical study. *China Ocean Eng.* **2013**, *27*, 615–628. [CrossRef]
23. Hyeon, J.W.; Cho, I.-H. Experimental Study on Sloshing in Rectangular Tank with Vertical Porous Baffle. *J. Ocean Eng. Technol.* **2015**, *29*, 291–299. [CrossRef]
24. Poguluri, S.K.; Cho, I.H. Liquid sloshing in a rectangular tank with vertical slotted porous screen: Based on analytical, numerical, and experimental approach. *Ocean Eng.* **2019**, *189*, 106373. [CrossRef]
25. Yu, L.; Xue, M.; Zheng, J. Experimental study of vertical slat screens effects on reducing shallow water sloshing in a tank under horizontal excitation with a wide frequency range. *Ocean Eng.* **2019**, *173*, 131–141. [CrossRef]
26. Nasar, T.; Sannasiraj, S.A.; Sundar, V. Performance assessment of porous baffle on liquid sloshing dynamics in a barge carrying liquid tank. *Ships Offshore Struct.* **2020**, *16*, 773–786. [CrossRef]

27. Gao, H.; Yin, Z.; Liu, J.; Zang, Q.; Lin, J. Finite element method for analyzing effects of porous baffle on liquid sloshing in the two-dimensional tanks. *Eng. Comput.* **2021**, *38*, 2105–2136. [CrossRef]
28. Wang, B.; Xu, T.; Jiang, Z.; Wang, S.; Dong, G.; Wang, T. Numerical simulation of sloshing flow in a 2D rectangular tank with porous baffles. *Ocean Eng.* **2022**, *256*, 111384. [CrossRef]
29. Nimisha, P.; Jayalekshmi, B.R.; Katta, V. Effect of Frequency Content of Seismic Excitation on Slosh Response of Liquid Tank with Baffle Plate. *J. Earthq. Tsunami* **2023**, *17*, 2350001. [CrossRef]
30. Nimisha, P.; Jayalekshmi, B.R.; Venkataramana, K. Effective configuration of perforated baffle plate for efficient slosh damping in liquid retaining tanks under lateral excitation. *Ocean Eng.* **2022**, *259*, 111855. [CrossRef]
31. Arun, G.; Cho, I.H. Anti-sloshing effects of a vertical porous baffle in a rolling rectangular tank. *Ocean Eng.* **2020**, *214*, 107871. [CrossRef]
32. Hirt, C.W.; Nichols, B.D. Volume of fluid (VOF) method for the dynamics of free boundaries. *J. Comput. Phys.* **1981**, *39*, 201–225. [CrossRef]
33. Osher, S.; Sethian, J.A. Fronts propagating with curvature-dependent speed: Algorithms based on Hamilton-Jacobi formulations. *J. Comput. Phys.* **1988**, *79*, 12–49. [CrossRef]
34. Boroomand, B.; Bazazzadeh, S.; Zandi, S.M. On the use of Laplace's equation for pressure and a mesh-free method for 3D simulation of nonlinear sloshing in tanks. *Ocean Eng.* **2016**, *122*, 54–67. [CrossRef]
35. Morteza, G.; Mahmoud, G. Numerical analysis of fully non-linear sloshing waves in an arbitrary shape tank by meshless method. *Eng. Anal. Bound. Elem.* **2022**, *144*, 366–369. [CrossRef]
36. Sun, X.; Zhong, Y.; Feng, B.; Liu, C.; Yin, Y. Numerical Computation of Sloshing-Induced Force in Complex Ship Tanks under the Excitation of Ship Rolling Motion Based on the MPS Method. *Appl. Sci.* **2022**, *12*, 5130. [CrossRef]
37. Lucy, L.B. A numerical approach to the testing of the fission hypothesis. *Astron. J.* **1977**, *82*, 1013. [CrossRef]
38. Gingold, R.A.; Monaghan, J.J. Smoothed particle hydrodynamics: Theory and application to non-spherical stars. *Mon. Not. R. Astron. Soc.* **1977**, *181*, 375–389. [CrossRef]
39. Koshizuka, S.; Oka, Y. Moving-Particle Semi-Implicit Method for Fragmentation of Incompressible Fluid. *Nucl. Sci. Eng.* **1996**, *123*, 421–434. [CrossRef]
40. Delorme, L.; Colagrossi, A.; Souto-Iglesias, A.; Zamora-Rodríguez, R.; Botía-Vera, E. A set of canonical problems in sloshing, Part I: Pressure field in forced roll—Comparison between experimental results and SPH. *Ocean Eng.* **2008**, *36*, 168–178. [CrossRef]
41. Zhang, G.; Zhao, W.; Cheng, W. Numerical simulations of sloshing waves in vertically excited square tank by improved MPS method. *J. Hydrodyn.* **2022**, *34*, 76–84. [CrossRef]
42. Sanchez-Mondragon, J.; Felix-Gonzalez, I.; Cruces-Giron, A.R. Turbulence analysis for vertical baffle configurations on prismatic tanks by the MPS method. *Ocean Eng.* **2022**, *264*, 112392. [CrossRef]
43. Wang, L.; Xu, M.; Zhang, Q. Numerical Investigation of Shallow Liquid Sloshing in a Baffled Tank and the Associated Damping Effect by BM-MPS Method. *J. Mar. Sci. Eng.* **2021**, *9*, 1110. [CrossRef]
44. Wang, L.; Khayyer, A.; Gotoh, H.; Jiang, Q.; Zhang, C. Enhancement of pressure calculation in projection-based particle methods by incorporation of background mesh scheme. *Appl. Ocean Res.* **2019**, *86*, 320–339. [CrossRef]
45. Khayyer, A.; Gotoh, H. Modified Moving Particle Semi-implicit methods for the prediction of 2D wave impact pressure. *Coast. Eng.* **2008**, *56*, 419–440. [CrossRef]
46. Tanaka, M.; Masunaga, T. Stabilization and smoothing of pressure in MPS method by Quasi-Compressibility. *J. Comput. Phys.* **2010**, *229*, 4279–4290. [CrossRef]
47. Wang, L.; Jiang, Q.; Zhang, C. Improvement of moving particle semi-implicit method for simulation of progressive water waves. *Int. J. Numer. Methods Fluids* **2017**, *85*, 69–89. [CrossRef]
48. Khayyer, A.; Gotoh, H. Enhancement of stability and accuracy of the moving particle semi-implicit method. *J. Comput. Phys.* **2011**, *230*, 3093–3118. [CrossRef]
49. Liu, X.; Morita, K. An advanced moving particle semi-implicit method for accurate and stable simulation of incompressible flows. *Comput. Methods Appl. Mech. Eng.* **2018**, *339*, 467–487. [CrossRef]